Plasma Science and Technology

PAPER

Sterilization mechanism of helium/helium–oxygen atmospheric-pressure pulsed dielectric barrier discharge on membrane surface

To cite this article: Xingyu CHEN *et al* 2022 *Plasma Sci. Technol.* **24** 124015

© 2022 Hefei Institutes of Physical Science, Chinese Academy of Sciences and IOP Publishing Printed in China and the UK Plasma Science and Technology

Plasma Sci. Technol. **24** (2022) 124015 (9pp) https://doi.org/10.1088/2058-6272/aca06e

Sterilization mechanism of helium/helium–oxygen atmospheric-pressure pulsed dielectric barrier discharge on membrane surface

Xingyu CHEN (陈星宇), Yuhan LI (李雨菡), Mengqi LI (李孟琦) and Zilan XIONG (熊紫兰)[*]

State Key Laboratory of Advanced Electromagnetic Engineering and Technology, Huazhong University of Science and Technology, Wuhan 430074, People's Republic of China

E-mail: zilanxiong@hust.edu.cn

Received 17 August 2022, revised 4 November 2022
Accepted for publication 4 November 2022
Published 14 December 2022

Abstract

Pulsed dielectric barrier discharge (PDBD) exhibits several applications in different fields; however, the interaction of its components with substances remains a key issue. In this study, we employed experimental and numerical modeling to investigate the interactions between different PDBD components and substances in pure helium and a helium–oxygen mixture. A membrane comprising a *Staphylococcus aureus* strain was utilized as the treatment object to demonstrate the trace actions of the evolutions and distributions of certain components on the surface of the substance. The results revealed that the shapes and sizes of the discharging area and inhibition zone differed between groups. Under a pure helium condition, a discharge layer existed along the membrane surface, lying beside the main discharging channel within the electrode area. Further, an annulus inhibition zone was formed at the outer edge of the electrode in the pure helium group at 30 s and 1 min, and this zone extended to a solid circle at 2 min with a radius that was ~50% larger than that of the electrode radius. Nevertheless, the discharging channel and inhibition zone in the helium–oxygen mixture were constrained inside the electrode area without forming any annulus. A 2D symmetrical model was developed with COMSOL to simulate the spatiotemporal distributions of different particles over the membrane surface, and the result demonstrated that the main components, which formed the annulus inhibition zone under the pure helium condition, contributed to the high concentration of the He^+ annulus that was formed at the outer edge of the electrode. Moreover, O^+ and O_2^+ were the main components that killed the bacteria under the helium–oxygen mixture conditions. These results reveal that the homogenization treatment on a material surface via PDBD is closely related to the treatment time and working gas.

Keywords: pulsed dielectric barrier discharge, interaction mechanism, numerical modeling, spatiotemporal distribution of species, treatment substance

(Some figures may appear in colour only in the online journal)

1. Introduction

Gas discharge at atmospheric pressure is an emerging plasma generation technology. Under certain conditions, this technology can generate a large-volume, uniform, and highly active nonequilibrium plasma. It is currently a research hotspot in the field of discharge and plasma [1–7]. Further, the development of pulse power technology has increased the wide utilization of atmospheric-pressure pulsed dielectric barrier discharge (PDBD) employing repetitive pulse voltage

---

[*] Author to whom any correspondence should be addressed.

as the excitation source. Compared with the phenomena in alternating current (AC) DBD, the ultrafast rising and falling edges in the pulse discharge process can rapidly generate ionization waves with higher electron energy. Thus, PDBD represents an energy-saving and efficient treatment method that is attracting increased attention [8–11].

Atmospheric-pressure PDBD exhibits abundant applications in different processes, such as material modification, wastewater/gas removal, and medical sterilization, as well as in the ozone industry [12–15], because of its rich ultraviolet (UV) rays, charged particles, high-energy electrons, and neutral particle contents in the metastable and excited states; it also contains different chemically active species. The discharge morphology and particle-density distributions of atmospheric-pressure PDBD are closely related to its applications, particularly in the treatment of substances. The shape and area of the discharge, as well as the generation of active components of the discharge in different gas components, and its electrical parameters directly affect the macroscopic characterization of PDBD, further affecting its interaction mechanism with the action object. For example, in the application of PDBD to bacterial sterilization, the main sterilization factors differ with the various discharge forms and different bacteria types. These factors can either combine or act separately to kill microorganisms. Sale and Hamilton systematically studied the effect of high-voltage pulsed electric field (PEF) technology on the sterilization process of microorganisms, demonstrating that the microorganisms were killed by the direct effect of the high-voltage PEF treatment and not by the increase in the electrolysis or temperature [16]. Laroussi *et al* studied the mechanism of the inactivation of *Bacillus subtilis* employing DBD plasma. They observed that the active particles played the most significant role among the influencing factors, such as the UV-active particles, as well as the thermal effect [17]. Heinlin *et al* confirmed that the local high-field strength, which is generated after the accumulation of charged particles on the cell surface, might disintegrate the cell and kill it [18]. Several related theoretical and applied research projects are ongoing, although the findings regarding the interaction mechanism between plasma and microorganisms still differ.

To obtain information on the amount or concentration of these components in cold atmospheric plasmas, special measurement methods were employed for each detection object [19–24]. However, the detection of the amount or spatiotemporal distribution of the concentration for each component in a complex DBD system exhibiting different electrical parameters and geometries is challenging. Numerical modeling represents another powerful tool for investigating the generated reactive species and spatiotemporal distribution of their number density in DBD. Wei *et al* established plasma and chemical models, which can elucidate the mechanism of species as well as the spatiotemporal distribution for ozone generation, to numerically study the spatiotemporal distribution of components and EFs in an oxygen parallel-plate positive PDBD [25]. Jiang *et al* explored the relationship among the properties of propagating streamers, the spatial distribution of active species, and the volatile organic compound-degradation performance of sliding DBD plasmas under different pulse-excitation conditions [26]. By integrating different plasma-chemistry, photoionization, and energy-loading models, Takana and Nishiyama performed a 2D numerical simulation of a high-energy-loaded nanosecond direct current (DC) PDBD in a methane–air mixture. The results revealed that an increased number density of oxygen radicals was generated by the energy to achieve plasma-assisted combustion [27]. Wang *et al* employed a 2D fluid model to investigate the properties of a multicurrent PDBD with ring electrodes in helium. The result revealed that the irregular accumulation of surface charges during previous discharges exerted different effects on the EF in the gas gap during subsequent discharges [28]. The studies of the EF and spatiotemporal distribution of particles were highly beneficial for understanding related experimental phenomena in PDBD. However, the existing numerical modeling studies mainly focused on the particle distribution and chemical reaction, and a detailed study on how the distribution of these components will function on the treatment object under different discharge conditions is still lacking.

In this study, we developed an experimental system and a 2D numerical model to investigate the interactions between the species generated by DC-PDBD and the treatment object. First, the DC-PDBD system was developed; a nitrocellulose membrane with a *Staphylococcus aureus* (*S. aureus*) strain on its surface was employed as the substance. The shapes of the colony under different treatment times and working gas conditions were employed as an indicator of the treatment effect. Thereafter, the evolution of the charged particles in the gas gap of atmospheric-pressure PDBD was analyzed via a COMSOL 2D symmetrical model. The motion laws of the charged particles in different gas environments were obtained, after which the correctness of the model was verified by comparing the simulation results of the voltage and current waveforms. Finally, the interaction mechanism of how PDBD acted on the treatment object was discussed.

2. Experimental and simulated models

2.1. Experimental setup

Figure 1 shows the schematic of the experiment. The platform of the experiment mainly comprised a pulse generator (PVX-4100, USA), a high voltage DC power supply (SL30PN300), a homemade DBD device, and measurement instruments. The amplitude was fixed at 5.8 kV and the frequency of the applied voltage was fixed at 8 kHz. The pulse width was 1 μs, while the rising and falling edges were both 50 ns during the experiments. A high-voltage probe (Tektronix P6015A) and current probe (Pearson 6585) were employed to measure the applied voltage and current, respectively, and the waveforms were recorded by an oscilloscope (Tektronix MDO3034).

The DBD device was mounted at the center of an acrylic cylindrical box (radius = 50 mm, height = 100 mm) as the treatment chamber. The electrode was produced from copper and exhibited good conductivity. The radius of each electrode

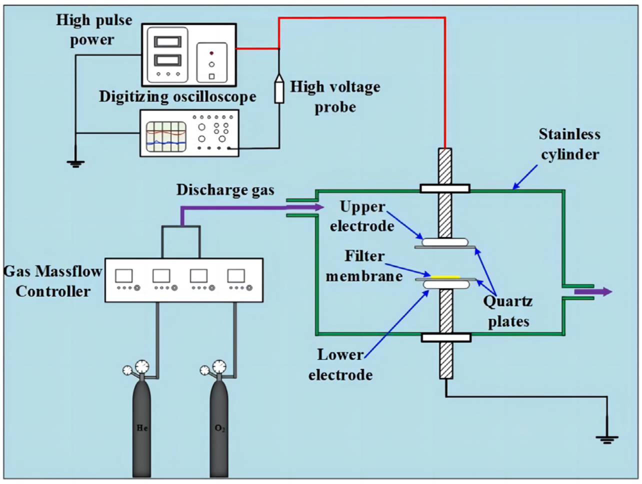

Figure 1. Experimental setup of PDBD.

was 12.5 mm. The upper and lower electrodes were covered with smooth and transparent quartz plates, respectively, with a radius of 40 mm and a thickness of 1.2 mm. A slice of the microporous filter membrane (radius and thickness are 25 and 0.12 mm, respectively) containing the *S. aureus* strain on its surface was placed in the center of the lower quartz plate during the treatment. The distance between the upper and lower quartz pieces (gas gap) was fixed at 5 mm. Pure helium or a mixture of helium and 1% oxygen was utilized as the working gas at a flow rate of 2 l min^{-1}. The working gas was continuously injected into the treatment chamber by a mass flow controller (MFC, D07–19B, 0–5 SLM).

2.2. Materials and treatments

S. aureus was cultured in a nutrient broth (NB), and the optical density of the bacterial solution was measured employing a UV–visible (UV–Vis) spectrometer (SpectraMaxM4) [29]. The concentration of the bacterial solution was cultured to approximately 1×10^9 cfu ml^{-1}, and then was diluted to 1×10^8 cfu ml^{-1}. Thereafter, the bacterial solution was shaken, after which 10 μl of it was pipetted onto the filter paper. Next, a sterilized cotton swab was employed to spread the bacterial solution uniformly across the entire membrane surface. Further, the membrane containing the bacterial strain was placed on the cathode of the electrode for treatment. The samples were divided into the following four groups: the control, air without discharge, He discharge, and He + O_2 discharge groups. The samples in each treatment group were treated for 30 s, 1 min, and 2 min, and the treatments were repeated three times under each condition.

The PDBD treatment procedure was as follows. First, the working gas was injected into the discharge chamber 2 min before the treatment to exhaust the air inside. Next, we turned on the pulsed DC power supply and set the parameters. After completing the set treatment time, we turned off the power supply to stop the discharge. Subsequently, we removed the treated membrane and placed it onto the agar culture plate. The plate was placed in the incubator for 18 h at 36 °C, and the bacterial colony distribution was recorded. The images of all the samples were taken before and after PDBD treatment. To demonstrate the pattern of the inhibition zone on the membrane, the color of the bacteria was changed from light yellow to blue by the Photoshop software.

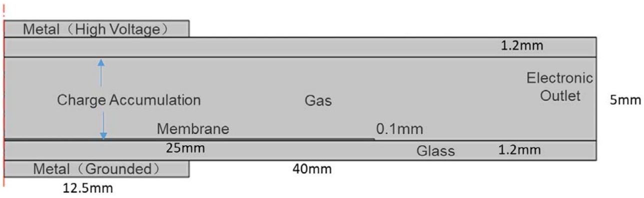

Figure 2. Schematic of the 2D symmetrical model.

2.3. Model development

Previous PDBD simulation studies mainly employed 1D models with relatively simple structures, and parameters in different regions that were the same distance from the electrode were considered consistent. The 1D model suited the steady-state process in which the air-gap distance is much smaller than the electrode size. Thus, to study the spatiotemporal distributions of the various particles, we employed a 2D symmetrical model following the device structure. The simulation of the plasma process mainly included a fluid model and a particle model. The fluid model treats the plasma as a charged gas cluster and analyzes it with an overall equation. Although the particle model simulates all the particles in the simulation area, it exhibits higher accuracy. However, it has a longer calculation time. Figure 2 shows the schematic of this model. The electrode, dielectric sheet, and filter membrane are cylinders exhibiting symmetrical structures; their sizes were set according to the real value. Additionally, the relative permittivity of the quartz plate was 3.7, while that of the gas was 1, which is considered the relative permittivity of vacuum. The filter membrane was relatively wet because it was coated with the bacteria, and its assumed relative permittivity was 2.6. After selecting the particle reaction, the discharge process was simulated based on the basic particle-diffusion equation and overall law.

2.4. Theoretical formula

The initial density, $n_{\mathrm{e}0}$, of the electrons was 10^{13} m^{-3} [30], and the initial velocity, μ, was 0; the relationship between their concentration and time satisfies the convection–diffusion equation as follows [31]:

$$\frac{\partial n_{\mathrm{e}}}{\partial_t} + \Delta \cdot \Gamma_{\mathrm{e}} = R_{\mathrm{e}} - (\mu \cdot \nabla) n_{\mathrm{e}}, \tag{1}$$

where Γ_{e} denotes the electron energy flux, which is employed to obtain the spatial distribution of the electron energy. The electron energy mobility and diffusivity are functions of the average electron energy, which is calculated employing the electron-collision cross-section data as follows:

$$\Gamma_{\mathrm{e}} = -(\mu_{\mathrm{e}} \cdot E) n_{\mathrm{e}} - D_{\mathrm{e}} \cdot \nabla n_{\mathrm{e}}, \tag{2}$$

where μ_{e} denotes the mobility of an electron with a value of 0.1131 $\mathrm{m}^2\,(\mathrm{V{\cdot}s})^{-1}$, D_{e} is 0, and E denotes the electric field

Table 1. He and O_2 are involved in the chemical reaction formula of the ns PDBD.

Reaction equation	Rate coefficient ($cm^3 s^{-1}$)	References
$e + He \rightarrow He^* + e$	$4.2 \times 10^{-9} T_e^{0.31} e^{-19.8/T_e}$	[32]
$e + He^* \rightarrow He + e$	2.9×10^{-9}	[33]
$e + He \rightarrow He^+ + 2e$	$1.5 \times 10^{-9} T_e^{0.68} e^{-24.6/T_e}$	[32]
$e + He^* \rightarrow He^+ + 2e$	$1.28 \times 10^{-7} T_e^{0.6} e^{-4.78/T_e}$	[32]
$He^* + He^* \rightarrow He^+ + He + e$	2.7×10^{-10}	[32]
$e + He^+ \rightarrow He$	$1.327 n_e \times 10^{-21} (T_e/T_g)^{-0.44}$	[32]
$e + O_2 \rightarrow O^- + O$	$8.8 \times 10^{-11} e^{-4.4/T_e}$	[34]
$e + O_2^+ \rightarrow O + O$	$2.2 \times 10^{-8} T_e^{-0.5}$	[34]
$e + O^- \rightarrow O + 2e$	$2.0 \times 10^{-7} e^{-5.5/T_e}$	[35]
$e + O_2 \rightarrow O^+ + O^- + e$	$7.1 \times 10^{-11} T_e^{0.5} e^{-17/T_e}$	[35]
$e + O_2 \rightarrow O^+ + O + 2e$	$5.3 \times 10^{-10} T_e^{0.9} e^{-20/T_e}$	[35]
$e + O_2 \rightarrow O + O + e$	$4.2 \times 10^{-9} e^{-5.6/T_e}$	[35]
$e + O_3 \rightarrow O_2^- + O$	1×10^{-9}	[35]
$e + O_3 \rightarrow O^- + O_2$	$9.3 \times 10^{-10} / T_e^{0.62}$	[36]
$e + O_3 \rightarrow O + O_2 + e$	$1.0 \times 10^{-8} (300/T_g)^{0.5}$	[36]
$e + O \rightarrow O^+ + 2e$	$9.0 \times 10^{-9} T_e^{0.7} e^{-13.6/T_e}$	[36]
$O^- + O_2 \rightarrow O_3 + e$	5.0×10^{-15}	[37]
$O^- + O_3 \rightarrow O_3^- + O$	5.3×10^{-10}	[38]
$O^- + O_2^+ \rightarrow 3O$	1.0×10^{-7}	[34]
$O_2^+ + O^- \rightarrow O + O_2$	$2.0 \times 10^{-7} (200/T_e)^{0.5}$	[35]
$O^+ + O^- \rightarrow 2O$	$2.0 \times 10^{-7} (300/T_e)^{0.5}$	[35]
$O_2^- + O^+ \rightarrow O + O_2$	$2.0 \times 10^{-7} (300/T_g)$	[37]
$O_2^- + O_2^+ \rightarrow 2O_2$	$2.0 \times 10^{-7} (300/T_g)$	[37]
$O_2^- + O_3 \rightarrow O_3^- + O_2$	$6.0 \times 10^{-10} (300/T_g)^{-0.5}$	[37]
$O^+ + O_2 \rightarrow O_2^+ + O$	2.0×10^{-11}	[35]
$O + O_3 \rightarrow 2O_2$	$1.5 \times 10^{-11} (2250/T_g)$	[39]
$O_3^- + O \rightarrow O_2^- + O_2$	2.0×10^{-7}	[40]
$O_3^- + O_2^+ \rightarrow O_3 + 2O$	3.2×10^{-10}	[37]
$He + O_3 \rightarrow O + O_2 + He$	2.28×10^{-26}	[40]
$He^* + O_2 \rightarrow O_2^+ + e + He$	$2.54 \times 10^{-10} (300/T_g)^{0.5}$	[37]

(EF) strength. The strong calculation of the EF forces everywhere was based on the Poisson equation as follows:

$$E = -\nabla V. \tag{3}$$

The electric displacement on the surface of the dielectric sheet satisfied the following equation:

$$D = \varepsilon E \tag{4}$$

where D denotes the electric displacement, and ε denotes the relative permittivity.

The charges accumulated on the surface of the dielectric sheet satisfied the following equation:

$$-n \cdot (D_1 - D_2) = \rho_s \tag{5}$$

where D_1 and D_2 denote the electric displacement of glass and gas, respectively.

The accumulation of the charges induced discharging, and the surface current density satisfied the following equation:

$$\frac{\rho_s}{\partial_t} = n \cdot J_e + n \cdot J_i, \tag{6}$$

where J_i and J_e denote the ion and electron current densities, respectively.

The gas components of the initial discharge were He and He–O_2, wherein there were several particle reactions. To conserve the computational time, only e, He^*, He^+, O, O_3, O^+, O^-, O_2^+, and O_2^- were regarded as the product, and the involved particle reactions and their rates are presented in table 1.

3. Results and discussion

3.1. Comparison of the voltages and currents in the experimental and simulation results

Figure 3 shows the discharging images and voltage/current waveforms of the experiment that was conducted in helium and the helium–oxygen mixture, and the simulated voltage and current waveforms are shown in figure 4. Positive and negative current pulses were generated at the rising and falling edges of the pulses, respectively. The experimentally measured current amplitude and change rule were consistent with the simulation results, indicating that the fluid model could be employed to simulate the DC-PDBD.

Figures 3(a1) and (b1) show that the discharging area was larger in pure helium than that in the helium–oxygen mixture.

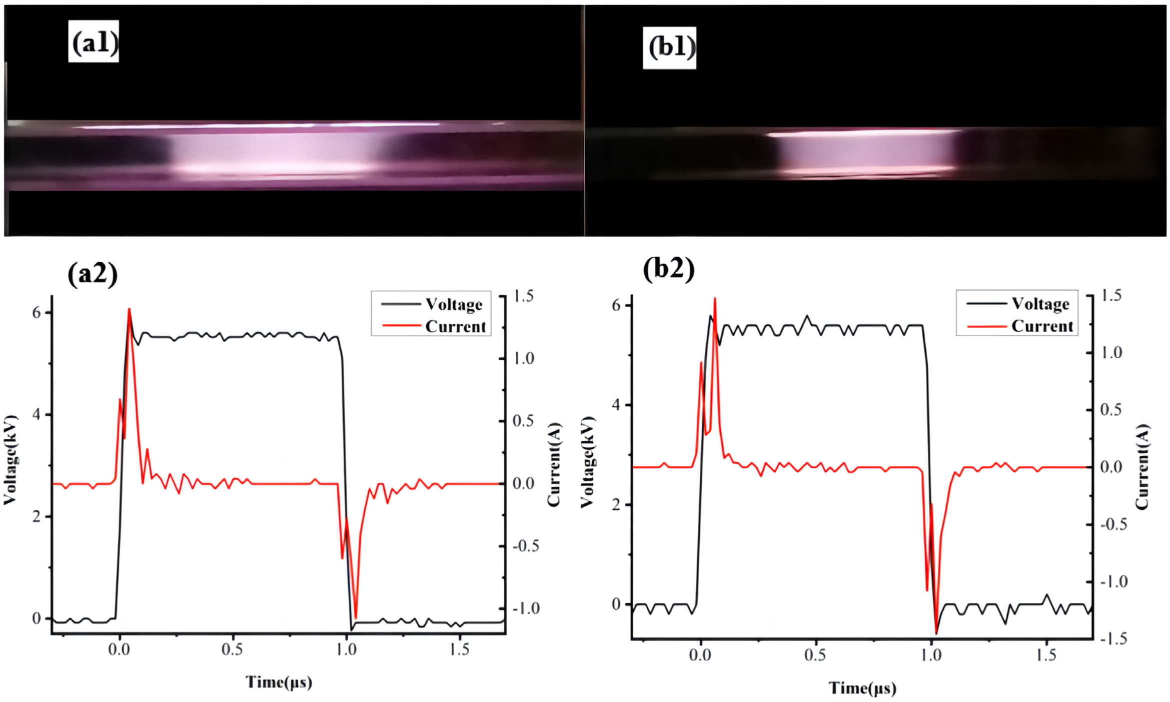

Figure 3. Discharging images and the measured voltage and current waveforms. (a1) Discharging process in helium and (a2) voltage and current waveforms in helium. (b1) Discharging process in the helium–oxygen mixture and (b2) voltage and current waveforms in the helium–oxygen mixture.

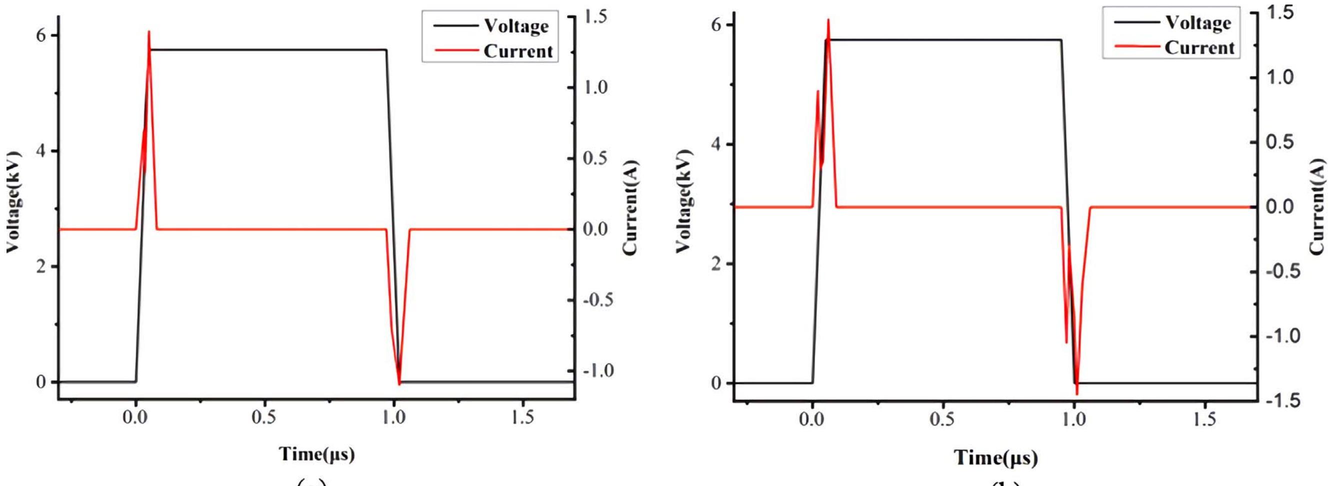

(a)

(b)

Figure 4. Simulated voltage and current waveforms in (a) helium and (b) helium–oxygen mixture.

The radius of the discharging channel in pure helium was 30% larger than that of the electrode (∼17.5 mm), and a strong glow was observed at the interface along the dielectric surface. When discharging in the helium–oxygen mixture, the discharge was mainly confined inside the electrode area. The radius of the discharging channel was generally the same as that of the electrode (∼12.5 mm). The glow at the interface between the gas and electrode plate/filter membrane was relatively weak.

3.2. Comparison of the sterilization effect

Figure 5 shows the effect of treating *S. aureus* in different gas environments. Figure 5(a) shows the effect for the blank control group. Under these conditions, the bacteria were uniformly distributed on the surface of the filter membrane. The group, which was named ‘air, power on’, was set up to investigate the effect of the external electrical field (figure 5(b)). Under this condition, the air gap could not be disintegrated and no discharge occurred. The field strength distribution in the air-gap area was the same as those in the helium and helium–oxygen mixed gas environments. The shape of the bacteria was still distributed uniformly on the surface of the filter membrane as in the control group, indicating that the influence of EF could be eliminated. Figure 5(c) shows the results of the discharging process in pure helium, and the process of developing the inhibition

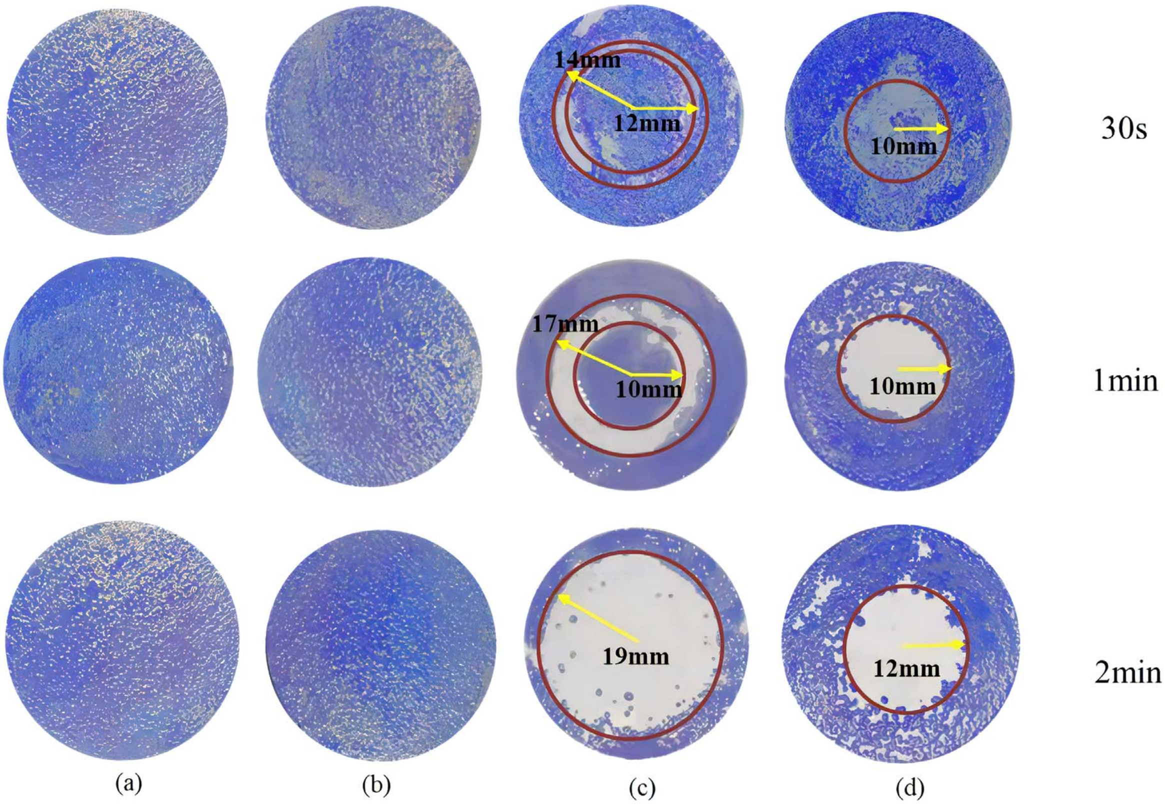

Figure 5. Inhibition zone of *S. aureus* on the membrane surface: (a) control, (b) air, power on, (c) pure helium, and (d) helium–oxygen mixture.

zone was observed. A 2-mm-wide annulus appeared outside the electrode area, and the bacteria outside this region were not killed. The width of the inhibition zone increased to ~7 mm at 1 min, and the radius of the inner zone decreased from ~12 to 10 mm, while the outer ring increased from 14 to 17 mm. After 2 min, the inhibition zone changed into a solid circle with a radius of 19 mm, which was approximately 50% larger than that of the electrode.

For the helium–oxygen mixture group (figure 5(d)), the inhibition zone was generally a solid circle within the electrode area, as was the case of the discharging column, and this differed from the observations in the pure helium group. The radius of the inhibition zone was only 70% of the electrode radius at 30 s, although it increased to a radius that was equivalent to that of the electrode after 2 min.

3.3. Discussion of the simulation results and mechanism

It is reported that the UV radiation in low temperature, atmospheric pressure discharge is weak and is not the main factor for sterilization [41–43]. Therefore, the effect of UV radiation could be ignored here. The temperatures of the electrode (measured by an infrared thermometer) in the helium and helium–oxygen mixture groups increased slightly (~1 °C) during the treatment. When the surrounding temperature was ~20 °C, the temperature change at the electrode did not affect the growth of the bacteria on the membrane.

Since factors such as the EF strength, UV radiation, and heat were not the main factors that affected the sterilization phenomenon, we concluded that the particles that were created by PDBD were the main factors. Several types of particles exist in plasma reactions, and further screening is required. Particle-induced plasma sterilization includes the following two aspects: (1) the neutral components cause the oxidization and apoptosis of the bacteria, and (2) the charged particles accumulate on the bacterial cell membrane to rupture their cell wall, causing apoptosis. To investigate the main factors that caused the different inhibition phenomena, we employed a 2D numerical model to study the particle density and spatiotemporal distribution over the membrane under the pure helium/helium–oxygen mixture conditions. In He and H_2/O_2 DBD discharge, the emissions from He (587.6, 667.8, 706.5 and 728.1 nm) and O (777.4 nm) are usually observed, and the related reactions are clear [44–46]. Under the pure helium condition, the effects of the charged particles, e and He^+, and neutral species, He^*, were mainly considered. Under the helium–oxygen mixture condition, the effects of neutral species, such as O and O_3, and charged particles, such as O^+, O_2^+, O^-, and O_2^-, were considered. Since the higher and lower particle concentrations of the various areas might differ by several orders of magnitude, each particle concentration was taken as the logarithm of base 10. To gain further insight into the particle distribution at the surface area for the formation of the inhibition zone, we only reported the results of 0.5 mm over the membrane surface.

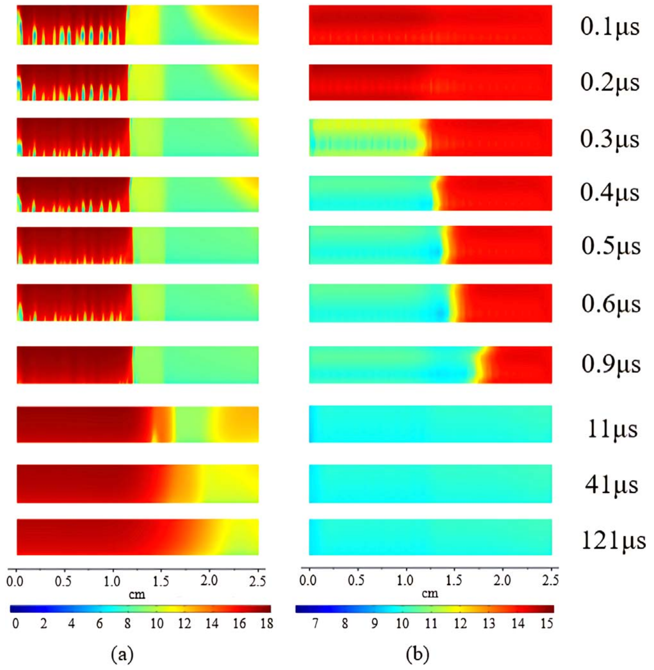

Figure 6. Logarithm results of the spatiotemporal distributions of the electron densities in the various working gases: (a) pure helium and (b) helium–oxygen mixture.

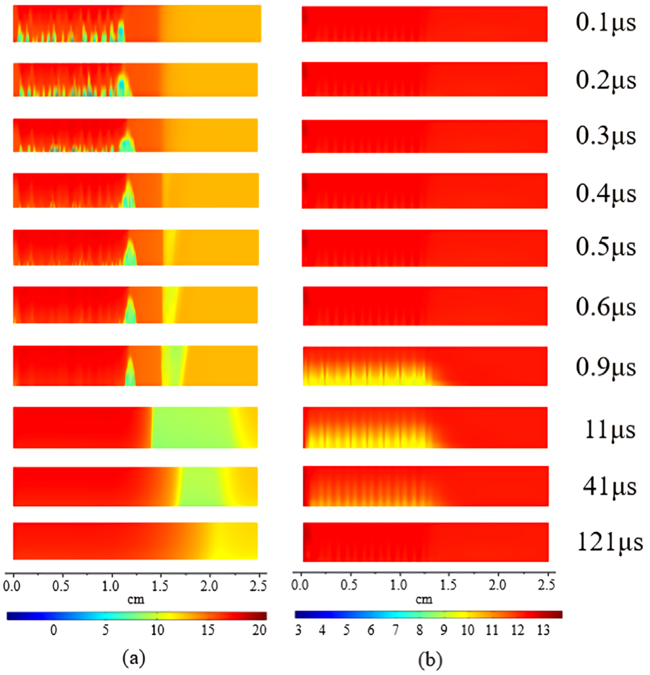

Figure 7. Logarithm results of the spatiotemporal distributions of He^+ density in the various working gases: (a) pure helium and (b) helium–oxygen mixture.

The logarithm results of the spatiotemporal distribution of the electron density in different working gases are shown in figure 6. In the pure helium group, the highest electron density over the membrane could reach $10^{18}\,m^{-3}$, which is similar to the results of [47]. The electron density at the membrane surface with the electrode area was lower than the initial value during the pulse-on stage (first 1 μs) under the pure helium condition. After turning off the pulse, the electrons diffused gradually to the outside area of the electrode, and the diffusion radius at 121 μs was up to ~19 mm, which was close to the size of the inhibition zone at 2 min in the pure helium group; however, the distribution shape of the electron could not explain the formation of the annulus area in the 30 s and 1 min groups. For the helium–oxygen mixture group, the electron concentration on the membrane surface was mainly constrained within the surface of the electrode, and it was more uniform than that in the pure helium group. Its highest electron density was 10^{15}–$10^{16}\,m^{-3}$, exhibiting a downward trend after 0.2 μs (10^{-4} times the initial conditions). This electron density was close to that obtained by Pan *et al* under similar conditions [48].

Further, the logarithm results of the spatiotemporal distribution of the He^+ density in different working gases are shown in figure 7. The evolution process of the He^+ number density was consistent with the development process of the bacteriostatic zone under the pure helium condition. The He^+ number density distribution was similar to the electron density distribution in the electrode area. The main difference was that a high concentration of the He^+ annulus appeared just around the outer edge area of the electrode during the pulse-on period, and as more than 100 times the initial concentration ($10^{15}\,m^{-3}$). The position and width of the He^+ annulus were almost the same as those of the inhibition annulus in the pure-helium group. The concentration of He^+ on the membrane surface within the electrode area was relatively low, but the applied EFs inside and on the outer edge of the electrode were relatively strong during the pulse-on period. The fringe EF outside the electrode edge and the accumulated He^+ particles combined to rapidly kill the bacteria in the annulus area. The annulus inhibition zone was formed following short-term plasma treatment. After turning off the pulse, the ions diffused gradually to the outer environment. The radius of the region exhibiting the final He^+ concentration was 100 times that of the initial value, corresponding to the radius of the discharging area along the membrane surface (~19 mm). After the long-term treatment, the inhibition zone gradually became a complete circle. The He^+ concentration in the helium–oxygen mixture group was even lower than that under the initial condition, and it did not exert any sterilization effect.

Figure 8 shows the logarithm results of the spatiotemporal distribution of the density of He^* in the various working gases. The number densities of He^* in pure helium and helium–oxygen mixture were relatively low, and they were uniformly distributed on the membrane surface; therefore, they were not the main bactericidal killing factor. Figure 9 shows the logarithm results of the spatiotemporal distribution of the neutral oxygen particle density in the helium–oxygen mixture. The oxygen was distributed over the entire surface area of the membrane where it was mainly consumed as a reactant. The density of O_3 remained uniform over the entire surface area of the membrane. Therefore, the neutral particles were not the main killing factors in the central inhibition zone in the helium–oxygen group.

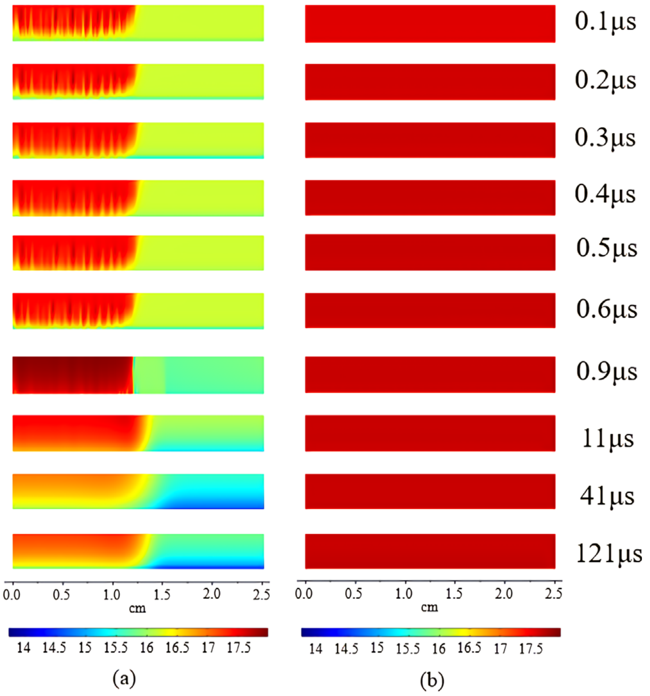

Figure 8. Logarithm results of the spatiotemporal distribution of He^* density in the different working gases: (a) pure helium and (b) helium–oxygen mixture.

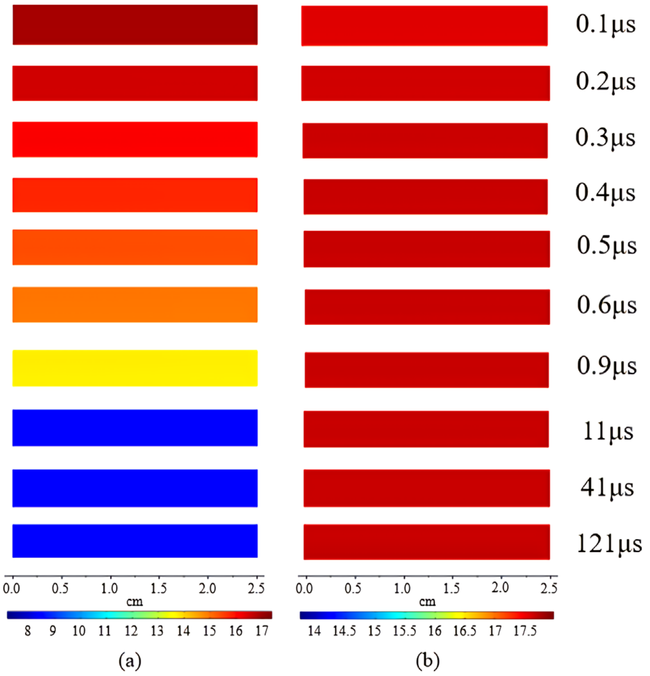

Figure 9. Logarithm results of the spatiotemporal distributions of the neutral particle densities in the helium–oxygen mixture: (a) O and (b) O_3.

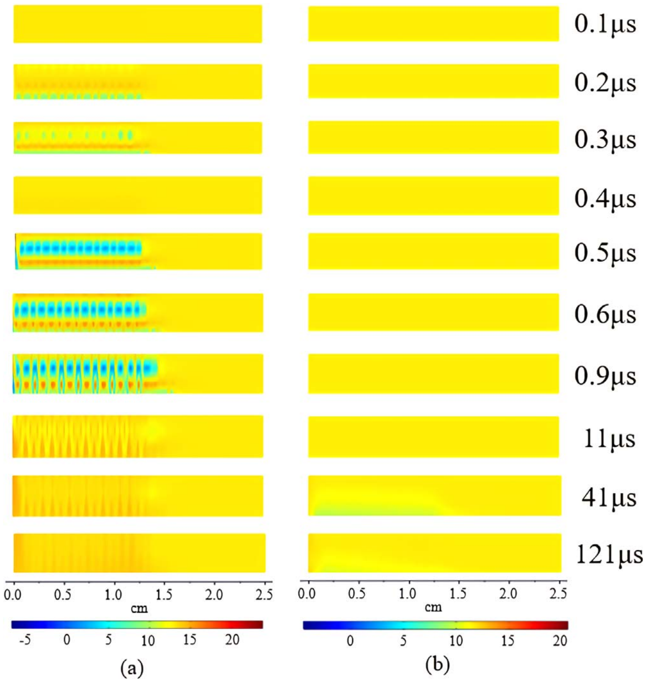

Figure 10. Logarithm results of the spatiotemporal distributions of the oxygen ion density in the helium–oxygen mixture: (a) O^+ and O_2^+, and (b) O^- and O_2^-.

Figure 10 shows the logarithm results of the spatiotemporal distribution of the oxygen ion density in the helium–oxygen mixture. The number density evolution process of the positively charged particles, such as O^+ and O_2^+, coincides with the development process of the inhibition zone in the helium–oxygen mixture group. Their densities on the membrane surface were higher within the electrode area during the pulse-on period, which was 100 times greater than the initial concentration. The distribution was not sufficiently uniform, accounting for the inhomogeneity of the shape of the inhibition zone, following the short-term treatment. At the pulse-off stage, the ions diffused gradually to the outer area of the electrode edge, but were mainly confined within the electrode area. The radius of the area (where the final concentrations of O^+ and O_2^+ were two orders greater than the initial value) was equivalent to the inhibition zone in the helium–oxygen mixture group, and this was slightly larger than the size of the electrode. It is well known that the oxidative free radicals such as O_2^- are strong scavengers in sterilization and important in the biological process [49], and their effectiveness depends on the dosage and how they act with the subject. In this case, the bacteria were spread on the membrane surface and the concentration of O^- and O_2^- over the membrane surface is relatively low, therefore, they did not contribute significantly to the killing process.

4. Conclusion

In this study, we investigated the spatiotemporal distributions of different particles in PDBD over the surface of a treatment object and explored the possible factors that contributed to the formation of the inhibition pattern in pure helium and helium–oxygen mixture. The discharge channel in pure helium was 30% larger than the radius of the electrode and comprised a layer of discharge along the dielectric surface exhibiting a radius of up to ~19 mm. An annulus inhibition zone was formed at 30 s and 1 min; additionally, the largest size extended to ~19 mm at 2 min during which a solid inhibition zone was formed. The discharge in the helium–oxygen mixture was constrained within the electrode area, and the size of the inhibition zone was almost the same as that of the electrode. The effects of EF, UV radiation, and temperature were ignorable in this case. The numerical modeling results demonstrated that the annulus inhibition zone in the helium discharge was mainly formed by the high concentration of the He^+ annulus, which was formed outside the edge area of the electrode. The higher concentrations of the positive oxygen ions (O^+ and O_2^+) than those of O^-, O_2^-, O, or O_3 played major roles in the helium–oxygen mixture group.

This investigation demonstrated that the homogenization treatment on a material surface via PDBD was closely related to the treatment time and working gases and the selection of the appropriate treatment condition was highly significant. The relationship between the inhibition pattern and particle distribution under other treatment conditions should be investigated in the future.

Acknowledgments

This work is supported by National Natural Science Foundation of China (No. 51907076) and the Interdisciplinary Fund of the Wuhan National High Magnetic Field Center (No. WHMFC202101).

References

[1] Xiong Z L *et al* 2021 *Plasma Process Polym.* **18** e2000204
[2] Wu S *et al* 2017 *Plasma Sources Sci. Technol.* **26** 09LT01
[3] Lee K *et al* 2006 *J. Microbiol.* **44** 269
[4] Kim B *et al* 2011 *Food Microbiol.* **28** 9
[5] Lu Y *et al* 2011 *Biochem. Eng. J.* **55** 17
[6] Khoja A H, Tahir M and Amin N A S 2019 *Energy Convers. Manage.* **183** 529
[7] Liu R Q *et al* 2021 *Chemosphere* **263** 127893
[8] Brandenburg R 2017 *Plasma Sources Sci. Technol.* **26** 053001
[9] Shao T *et al* 2008 *J. Phys. D: Appl. Phys.* **41** 215203
[10] Obradović B M, Sretenović G B and Kuraica M M 2011 *J. Hazard. Mater.* **185** 1280
[11] Massima Mouele E S *et al* 2021 *J. Environ. Chem. Eng.* **9** 105758
[12] Niu Z *et al* 2013 *Surf. Coat. Technol.* **228** S578
[13] Huang Y F *et al* 2016 *IEEE Trans. Plasma Sci.* **44** 938
[14] Von Woedtke T *et al* 2013 *Phys. Rep.* **530** 291
[15] Wei L S *et al* 2016 *Plasma Sci. Technol.* **18** 147
[16] Hamilton W A and Sale A J H 1967 *Biochim. Biophys. Acta - Gen. Subj.* **148** 789
[17] Laroussi M, Richardson J P and Dobbs F C 2002 *Appl. Phys. Lett.* **81** 772
[18] Heinlin J *et al* 2011 *J. Eur. Acad. Dermatol. Venereol.* **25** 1
[19] Reuter S *et al* 2015 *Plasma Sources Sci. Technol.* **24** 054001
[20] Winter J *et al* 2012 *J. Phys. D: Appl. Phys.* **45** 385201
[21] Nikiforov A Y *et al* 2015 *Plasma Sources Sci. Technol.* **24** 034001
[22] Hübner S *et al* 2015 *Plasma Sources Sci. Technol.* **24** 054005
[23] Wu S *et al* 2016 *Phys. Plasmas* **23** 103506
[24] Shu Z *et al* 2021 *Plasma Sources Sci. Technol.* **30** 055001
[25] Wei L S *et al* 2016 *Vacuum* **125** 123
[26] Jiang N *et al* 2018 *Chem. Eng. J.* **350** 12
[27] Takana H and Nishiyama H 2014 *Plasma Sources Sci. Technol.* **3** 034001
[28] Wang J *et al* 2020 *Phys. Plasmas* **27** 043501
[29] Liao X Y *et al* 2018 *J. Food Sci.* **83** 401
[30] Shi H, Wang Y H and Wang D Z 2008 *Phys. Plasmas* **15** 122306
[31] Sigmond R S 1984 *J. Appl. Phys.* **56** 1355
[32] Rauf S and Kushner M J 1999 *J. Appl. Phys.* **85** 3460
[33] Wang Q, Economou D J and Donnelly V M 2006 *J. Appl. Phys.* **100** 023301
[34] Deloche R *et al* 1976 *Phys. Rev. A* **13** 1140
[35] Gadri R B 1999 *IEEE Trans. Plasma Sci.* **27** 36
[36] Léveillé V and Coulombe S 2005 *Plasma Sources Sci. Technol.* **14** 467
[37] Gudmundsson J T *et al* 2001 *J. Phys. D: Appl. Phys.* **34** 1100
[38] Stafford D S and Kushner M J 2004 *J. Appl. Phys.* **96** 2451
[39] Atkinson R *et al* 1997 *J. Phys. Chem. Ref. Data* **26** 1329
[40] Lee D *et al* 2005 *IEEE Trans. Plasma Sci.* **33** 949
[41] Lu X P *et al* 2008 *J. Appl. Phys.* **104** 053309
[42] Dobrynin D *et al* 2011 *New J. Phys.* **13** 103033
[43] Laroussi M and Leipold F 2004 *Int. J. Mass Spectrom.* **233** 81
[44] Ricard A, Décomps P and Massines F 1999 *Surf. Coat. Technol.* **112** 1
[45] Liu Y G, Hao Y P and Zheng B 2012 *Phys. Plasmas* **19** 093506
[46] Nersisyan G and Graham W G 2004 *Plasma Sources Sci. Technol.* **13** 582
[47] Simeni M S *et al* 2021 *Plasma Sources Sci. Technol.* **30** 055004
[48] Pan G S *et al* 2016 *Phys. Plasmas* **23** 043508
[49] Graves D B 2012 *J. Phys. D: Appl. Phys.* **45** 263001